$3D + t$ Morphological Processing: Applications to Embryogenesis Image Analysis

Miguel A. Luengo-Oroz, David Pastor-Escuredo, Carlos Castro-Gonzalez, Emmanuel Faure, Thierry Savy, Benoit Lombardot, Jose L. Rubio-Guivernau, Louise Duloquin, Maria J. Ledesma-Carbayo, Paul Bourgine, Nadine Peyrieras, and Andres Santos

***Abstract*— We propose to directly process $3D+t$ image sequences with mathematical morphology operators, using a new classification of the $3D+t$ structuring elements. Several methods (filtering, tracking, segmentation) dedicated to the analysis of $3D + t$ datasets of zebrafish embryogenesis are introduced and validated through a synthetic dataset. Then, we illustrate the application of these methods to the analysis of datasets of zebrafish early development acquired with various microscopy techniques. This processing paradigm produces spatio-temporal coherent results as it benefits from the intrinsic redundancy of the temporal dimension, and minimizes the needs for human intervention in semi-automatic algorithms.**

***Index Terms*— $3D + t$ mathematical morphology, *in-vivo* light microscopy, spatio-temporal structuring elements, zebrafish embryogenesis.**

I. Introduction

THE ROLE OF automated image processing methods is crucial for the analysis of new biological data based on *in-vivo* imaging observations. Developmental biology is under revolution with the inclusion of new microscopy technologies [1] and automated processing methods [2]. In this context, image analysis is still an open challenge: new methodologies applied to *in-vivo* imaging should provide a set of tools able to deal with very different types of datasets [3]. The zebrafish a vertebrate which has phylogenetic proximity to humans is a reference model in developmental biology [4] and in the study of cancer and stem cells [5]. Thanks to the transparency of its tissue, it is possible to acquire high resolution *in-vivo* images of cell nuclei, cell membranes or gene expression during embryo development. Nevertheless, the massive quantity of data produced by this type of imaging from 2 to 50 000 cells in 24 h needs new automated strategies for data processing and interpretation. The ultimate goal in this context is to be able to perform the *in-toto* reconstruction of the whole specimen during its development [6]. That means the digitalization of each cell in time and space, leading to the cell lineage tree *sequencing* [7]–[9]. To this end, there are several microscopy imaging systems well suited for *in-vivo* imaging at cellular scale, such as two-photon laser scanning microscopy (LSM) [10], light sheet fluorescence microscopy (LSFM) [7] or multiharmonic imaging [11]. All these systems may obtain various channels, typically showing cell nuclei and/or cell membranes during embryo development. Because of the complexity of membrane images, nuclei are generally used to perform the tracking (reconstructing the lineage tree) and as the seed for membranes segmentation (that provide structural information). Usually tracking and segmentation methods for living cells analyze separately the 3D images of a time-lapse and rely on the same global strategy [12]: preprocessing image data, detecting individual particles per time point, linking particles along successive time points, and segmenting structures for further analysis. Hereafter, we briefly review existent literature. Nonlinear filtering techniques are usually chosen for preprocessing, e.g., PDE and variational formulations [13] or wavelet-domain thresholding techniques [14]. There exists a rich literature on biological spot detection, including morphological top-hat operators [15] or the discrete wavelet transform [16]. Concerning cell detection on LSM imaging of embryo development, advection-diffusion equations are an interesting option [17]. In order to perform the lineage tree reconstruction, detected cells should be linked along time [18]. For this purpose, the combinatorial problem of matching cells along time steps should be solved by deciding a strategy that balances between local and global optimization techniques [19] and incorporating contextual topological information, e.g., using level sets approaches [20]. Several methods on image segmentation have been adapted to cell biology problems, e.g., active contours [21] or graph-optimization [22]. In embryogenesis imaging, a region growing method can be applied for membrane segmentation starting from the detected cell center [23]. In [24], we found the comparisons of

Manuscript received February 2, 2011; revised January 15, 2012; accepted April 5, 2012. Date of publication May 1, 2012; date of current version July 18, 2012. This work was supported in part by the European Regional Development Funds and the FP6 NEST Program, AMIT-CDTI, TEC2010-21619-C04-03, and PRECISION (Spanish Ministry of Science), the French National Research Agency, and the PICATA Program of the Moncloa Campus of International Excellence, Spain. The associate editor coordinating the review of this manuscript and approving it for publication was Prof. David S. Taubman.

M. A. Luengo-Oroz, D. Pastor-Escuredo, C. Castro-Gonzalez, J. L. Rubio-Guivernau, M. J. Ledesma-Carbayo, and A. Santos are with Biomedical Image Technologies Laboratory, ETSI Telecomunicación, Universidad Politécnica de Madrid, Biomedical Research Center in Bioengineering Biomaterials and Nanomedicine (CIBER-BBN), Zaragoza 50018, Spain, and also with CEI Moncloa UCM-UPM, Madrid 28040, Spain (e-mail: maluengo@die.upm.es; david.pastor@die.upm.es; ccastro@die.upm.es; jlrubio@die.upm.es; mledesma@die.upm.es; andres@die.upm.es).

E. Faure, T. Savy, B. Lombardot, and P. Bourgine are with the Centre de Recherche en Epistemologie Appliquee, Ecole Polytechnique, CNRS, Paris 75016, France (e-mail: thierry.savy@polytechnique.edu; Emmanuel.faure@polytechnique.edu; benoit.lombardot@polytechnique.edu; paul.bourgine@polytechnique.edu).

L. Duloquin and N. Peyrieras are with the Neurobiologie et Developpement, Institut de Neurobiologie Alfred Fessard, CNRS, Gif/Yvette 91198, France (e-mail: louise.duloquin@gmail.com; nadine.peyrieras@inaf.cnrs-gif.fr).

Color versions of one or more of the figures in this paper are available online at http://ieeexplore.ieee.org.

Digital Object Identifier 10.1109/TIP.2012.2197007

2D segmentation methods for zebrafish embryo heart image sequences. Generic biological processing packages, such as Icy [25], Fiji or Imaris provide useful tools for tracking [26] and segmentation, the main drawback being the quantity of parameters to be tuned for the analysis of particular datasets.

Despite the extensive literature that approaches lineage reconstruction starting from the analysis of individual 3D images, just a few methods have really addressed particle tracking in a spatiotemporal integrated way [27], which is one the main goals of this research. Efforts in segmenting 4-D shapes have been made in cardiac imaging using 4-D active shapes [28]. In [29], the mechanical function of the left ventricle is assessed using 4-D deformable models. Regarding cell imaging, in [30], the evolution of the cell envelope during mitosis in 4-D confocal images has been analyzed with a deformable surface model. However, methods that process directly the 4-D datasets have not been mainstreamed because of the novelty of the microscopy techniques, the huge size of embryogenesis datasets (current (x, y, z, t) acquisitions are in the order of $\sim 10-100$ Gigabytes per dataset) and the complexity of the validation stage that requires interacting with complex $3D+t$ data.

Because of the inherent $3D+t$ nature of the data which is not fully exploited when analyzing separately 3D images and the requirement of straightforward, fast, and efficient algorithms to analyze massive data produced by the new microscopy technologies, this paper proposes a general $3D+t$ mathematical morphology approach for analysis based on the definition of extended forms of connectivity spatio-temporal structuring elements and assess its suitability through different methods applied to $3D+t$ synthetic and real datasets. Preliminary versions of some of the methods presented in this paper were drafted in [31] and [32]. Section II introduces the classification of the spatio-temporal structuring elements. Section III adapts morphological operators to the $3D+t$ domain and validates its use in a synthetic dataset. Section IV shows application examples in *in-vivo* image data of zebrafish embryogenesis. This paper is concluded in Section V.

II. $3D+t$ Processing Through Spatio-Temporal Structuring Elements

A. Background

Mathematical morphology is based on the application of lattice theory to spatial structures. Automated cytological analysis was one of the first biomedical image applications of mathematical morphology [33]. Numerous efficient methods have been described in the literature regarding cell segmentation either in 2D [34], [35] or 3D data [36]. Some applications have been developed to study spatio-temporal data, mainly in $2D+t$ for video analysis [37]. For $3D+t$ morphological processing, there are just a few examples devoted to the analysis of cardiac images [38], [39]. These contributions are based on the use of trivial expansions of the classical structuring elements to one more dimension (t) not considering that there is no direct correspondence between spatial connectivity (i.e., measured in micrometers) with temporal connectivity (i.e., measured in minutes). However, the analysis of spatio-temporal data requires novel forms of connectivity where the temporal connectivity is well suited to characterize the kinematics of the structures in this domain (hyper-structures).

	Isotropic	*Anisotropic*
Convex	The disk	The segment
Non-convex	The circle, i.e. the boundary of the disk.	Aligned points; in particular the couple of points, i.e. the boundary of the segment in $\Re^1$.

Fig. 1. Structuring elements classification according to *Serra* [40]. Anisotropy and convexity of spatial SEs are the main characteristics for this classification.

B. Spatio-Temporal Structuring Elements

Structuring elements SEs are used as kernels for different operators based on the two basic morphological operators dilation and erosion. According to *Serra* [40], structuring elements tell us about either the size or the spatial distribution of an object. Based on these features morphology and distribution, SEs can be classified according to whether they relate to objects size (convex) or spatial distribution (nonconvex) and whether they act equally in all spatial directions (isotropic) or not (anisotropic), see Fig. 1. However, as we broadened this classification to $3D+t$, we noted that a trivial expansion of these concepts into 4-D was not sufficient to tackle spatio-temporal phenomenology. Consequently, we decoupled space and time: convexity/nonconvexity and isotropy/anisotropy applied to both the spatial and temporal dimension produce a new classification that generates 16 types of SEs, see the table in Fig. 2). In this framework, SEs characterize the shape, the spatial distribution, and the temporal distribution or kinematics. Thus, morphological operators can be used to analyze the dynamic properties of the objects as periodicity or speed depending on the spatio-temporal coherence of the data. Hereafter, we describe some instances and characteristics of the different families of SEs generated by this classification.

1) SE_1 structuring elements include the *Hyper-Cylinder* or the *Hyper-Line* [see Fig. 2(a) and (b)].
2) SE_2 structuring elements can be derived from SE_1 instances restricting the construction to *causal or anti-causal* structures [see Fig. 2(c) and (d)], *deformations in time* [see Fig. 2(e)–(g)] or *trajectory twists* [see Fig. 2(h)].
3) SE_3 structuring elements include the *Hyper-Plane* or the *Hyper-Ellipsoid* [see Fig. 2(i) and (j)].
4) SE_4 structuring elements can be derived from SE_3 instances applying either *causality/anti-causality*, *deformations in time* or *trajectory twists*, such as the *Hyper-Helix* [see Fig. 2(k)].
5) SE_5 structuring elements can be derived as *time interpolators* of SE_1 instances [see Fig. 2(l)]. This structuring elements allow to choose at which temporal sampling rate the morphological operators are performed. They are useful when working with periodic signals.
6) SE_6, SE_7, and SE_8 structuring elements are the *time interpolated* versions of SE_2, SE_3, and SE_4, respectively.

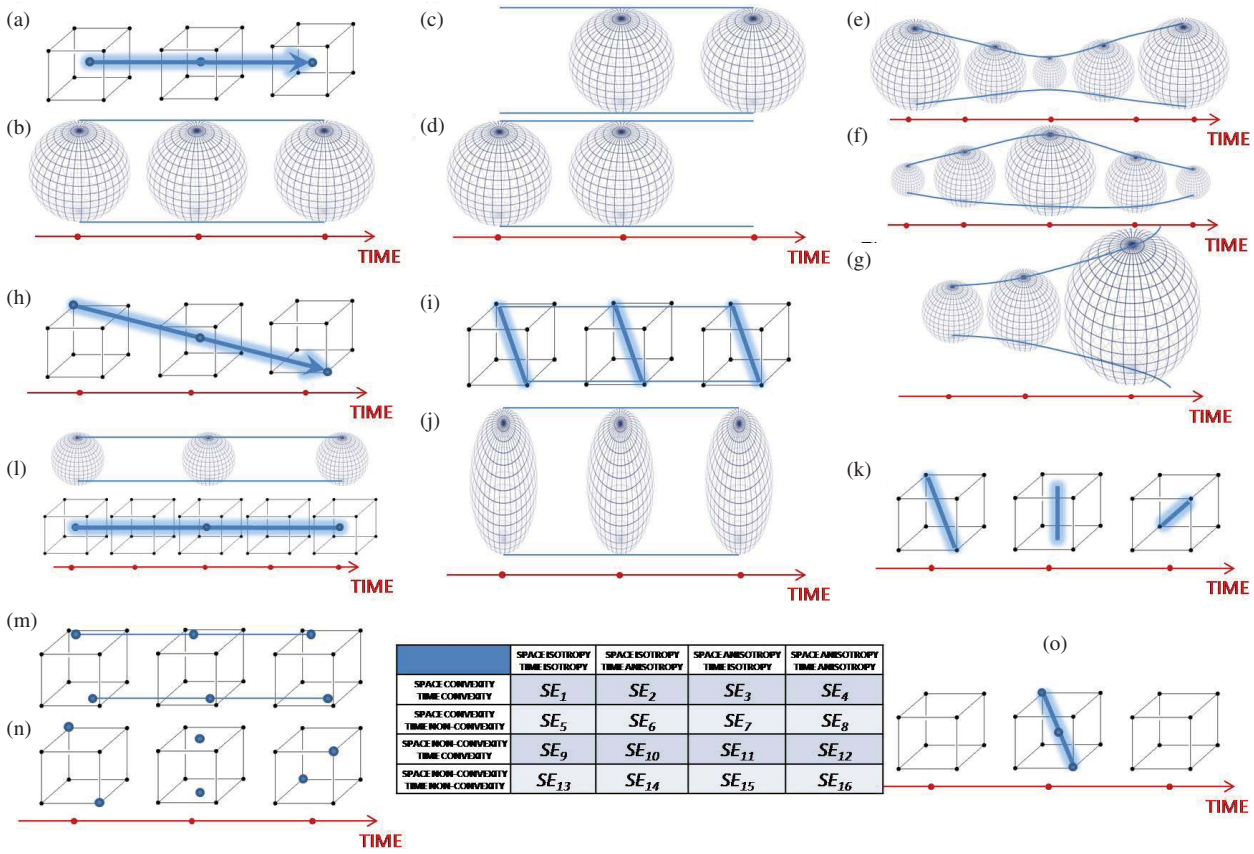

Fig. 2. Spatio-temporal structuring elements (SE_i) classification decoupling time/space connectivities. The classification is hereby broadened depending also on the isotropy and convexity of the temporal domain. The SEs used in this paper fall consistently under this classification. *Isotropic and convex* SEs, both in time and space, include (a) *Hyper-Line* and (b) *Hyper-Cylinder*. They can be employed to get useful insight on the trajectory of objects that can be considered a continuous hyper-structure along time (see Section III-C). (c) and (d) *Causal and anti-causal* SEs are particular instances of time anisotropy. They are extremely useful in order to restrict morphological operations to future/past events. Deformations along time produce *time-anisotropic* SEs, such as (e) *Hyper-Bow Tie*. (f) *Hyper-Sphere* or (g) *Hyper-Horn*. They can be designed based on contextual information of the application (e.g., *Hyper-Horns* can be useful to track quick changes of increasingly-distant trajectories, such as cell mitosis). (h) *Trajectory twists* also lead to SEs cases of time anisotropy. *Spatially anisotropic* instances of SEs include (i) *Hyper-Planes*, temporal successions of one segment, or (j) *Hyper-Ellipsoids*, which can be useful when dealing with images with poor z-resolution. (k) *Hyper-Helix* is an instance of a convex and anisotropic SE both in time and space. *Nonconvex in time* SEs are (l) *time interpolators*, allowing to choose at which temporal sampling rate the morphological operators are performed. They are useful to select a temporal scale to detect objects in a certain position finding out periodic phenomena. *Nonconvex in space* SEs are *space interpolators*. Particular instances are the (m) *Hyper-Parallel Lines*, isotropic in time, or (n) *Hyper-Solenoid* and (o) *Hyper-Points*, anisotropic in time. As in Serra's classification, they can be used to characterize spatial distribution of objects and how they reorganize in time.

7) SE_9, SE_{10}, SE_{11}, and SE_{12} structuring elements are hollow versions of SE_1, SE_2, SE_3, and SE_4, respectively. The *Hyper-Parallel Lines* or the *Hyper-Solenoid*, for instance, are particular examples of SE_{11} and SE_{12} types [see Fig. 2(m) and (n)].
8) SE_{13}, SE_{14}, SE_{15}, and SE_{16} structuring elements are the *time interpolated* versions of SE_9, SE_{10}, SE_{11}, and SE_{12}, respectively. For instance the *Hyper-Points* [see Fig. 2(o)].

III. $3D+t$ Analysis of Embryogenetic Hyper-Structures: Validation on Synthetic Data

In this section, we illustrate the overall morphological processing paradigm on $3D+t$ data. We have focused on the embryogenesis domain where both structural and dynamic information are of high interest. In order to validate the approach, we have created and used a $3D+t$ synthetic embryogenetic dataset where we could quantitatively assess the impact that working on the spatio-temporal domain brings in terms of efficiency and performance. In particular, four methodologies are introduced: $3D+t$ filtering of oriented hyper-objects, $3D+t$ reconstruction of hyper-structures, $3D+t$ watershed, and $3D+t$ skeletonization.

A. Synthetic Embryogenetic Dataset

We designed and created a synthetic $3D+t$ dataset that serves as the gold standard to evaluate the performance of the proposed methodologies based on $3D+t$ processing. This synthetic dataset was designed to mimic the features found in *in-vivo* acquisitions of embryogenesis. Three types of objects that can be tackled by the $3D+t$ techniques have been artificially reproduced: 1) nuclei trajectories; 2) cell membranes confining these trajectories; and 3) volumes of genetic expression held by the embryo cells and evolving over time, see Fig. 3. To recreate nuclei trajectories, we duplicated the true cell positions extracted from the analysis of time-lapse series spanning 30 min of the early development of an *amphioxus* embryo, a common animal model. Cell membranes were simulated by a Voronoi diagram [41] associated to the

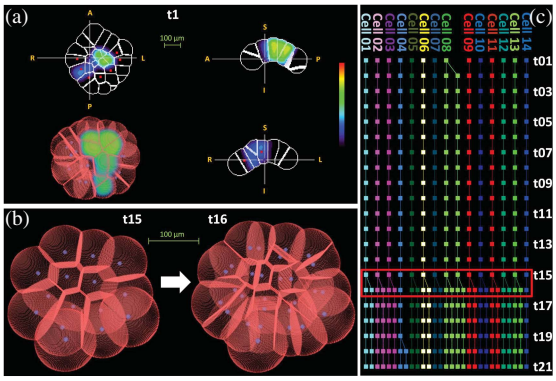

Fig. 3. (a) Synthetic dataset at t1 displaying the cell nuclei, membranes, and gene expression; *from top left, clockwise:* transversal, coronal and sagittal views, and volume rendering. (b) and (c) Representation of the synthetic cell lineage tree for 21 time steps. Cell divisions take place synchronously at t15 imitating the early embryogenesis behavior of animal models like *amphioxus*.

nuclei positions at each time step. This Voronoi diagram was bounded by the external embryo layer placed at the typical cell-to-cell distance from the outer nuclei tier. Finally, the artificial gene expression was created following a smoothed *"on–off"* propagation model, which affects different cell volumes through time. As a result, we generated an artificial model with spatial resolution $0.52 \times 0.52 \times 1.04$ μm^3 and temporal resolution $\Delta t = 1$ min 21 s comprising 21 frames of $512 \times 512 \times 128$ voxels. At first, there are 14 nuclei, which undergo at least one mitosis each, most of them synchronously, yielding a total of 29 cells by the end of the experiment (see Fig. 3).[1] This original data has been used to validate and illustrate the scope of the proposed $3D+t$ processing methodology for each particular method as described in the corresponding sections. The synthetic dataset is available online[1] to grant future comparisons against the same gold standard.

B. Twister Filtering for Oriented Hyper-Structures

1) Description: Time anisotropy in a structuring element (see Fig. 2) can be used to study object dynamics, e.g., a granulometric study with several structuring elements oriented in various angles can characterize object trajectories. In particular, we present here a filtering method based on morphological openings that removes temporally-inconsistent noise from $3D + t$ images in a very efficient way, with a predictable computational cost. A morphological opening with structuring element B, γ_B (from now on we use the notation from [42]), filters out bright structures from the images according to the predefined size and shape criterion of the structuring element (the behavior of closings may be inferred by duality). Any supremum of openings is an opening, allowing to extract specific geometrical structures of different classes in the same filtering processing. The operation $\Gamma^l_{n,d} = \vee_{i\in[1,d]}\gamma_{l^i_n}$ is an opening by line segments (see Fig. 2), where l^1_n, l^2_n, l^3_n, and l^4_n denote line segments of length n and respective orientation $0°, 45°, 90°, 135°$. For this experiment, we extended this filtering process to the spatio-temporal domain allowing all the possible rotations of a hyper-line segment SE (the angle of rotation is limited by the sampling rate and dimensions of the SE [43]). A hyper-line segment SE in $3D + t$ can be thought in different ways: a point that moves in a straight direction over time from *past* to *future*, a fixed point over time or a segment in the 3D space in the *present* time [see Fig. 2(a), (h), (o)]. For the sake of simplicity, in this experiment we use a rotation angle of 45°, so the number of possible orientations in a nD space is the number of boundary pixels in a 3^n box divided by 2. In 2D, if the initial orientation of segment l^1_n is 0^0 and we permit a rotation angle of 45°, there exists four possible segments l^1_n, l^2_n, l^3_n, and l^4_n, where l^i_n is rotated 45° from $l^{(i+1)|4}_n$ so $\sharp l(\dim = 2) = 4$. In these conditions, the opening by twister line segment is $\Gamma^l_{n,4} = \vee_{i\in[1,4]}\gamma_{l^i_n}$. In 3D, the interpretation remains the same as in the plane: we may extract all the lines with specific directions embedded in the 3D space. A rotation angle of 45° provides 13 possible orientations $\sharp l(\dim = 3) = 13$. In $3D+t$, the twister hyper-segment captures the displacements of the spatial structures if the temporal resolution is high enough, providing 40 segments with a rotation angle of 45°, $\sharp l(\dim = 4) = 40$.

2) Experiments on Synthetic Data: To validate this filtering method, we have applied it to the membranes in the synthetic data as they are hyper-structures that can be deformed in different directions along time. We have first downsampled our synthetic dataset to make it spatially isotropic $-1.04 \times 1.04 \times 1.04$ μm^3. Then, we have contaminated the artificial membranes with uncorrelated Gaussian noise of mean 0 and SNR 3.7 dB. The results of the twister $3D+t$ morphological opening are quantitatively compared against a Perona–Malik 3D filtering [44]. The twister structuring elements size is set to be $7 \times 7 \times 7 \times 3$ pixels. Perona–Malik is executed with typical parameters [45], four iterations, an integration constant set to 3/44, 70 as gradient modulus threshold and conduction coefficients chosen to privilege high-contrast edges over low-contrast ones. We have used the Hausdorff distance and the mean Hausdorff distance [23] as the metrics to evaluate the outcome of both techniques against the synthetic gold standard (see Fig. 4). The results show that both methods perform equally well, obtaining mean Haussdorff distances of 0.09 and 0.14 voxel units for the Perona–Malik and twister filter, respectively. In terms of efficiency however, the twister filtering performs around 30% faster than Perona–Malik. The main limitation of the twister methodology would eventually come from the temporal resolution of the dataset, as longer time steps would require longer segments and less flexibility to capture structure orientations with an optimal number of twister elements. Future comparisons of this strategy with other recently published methodologies in the field of embryogenesis, including [13] and [46] would be of interest.

C. Highlighting Hyper-Structures

1) Description: The morphological reconstruction operator [47] using spatio-temporal structuring elements allows the highlighting of a hyper-structure over the whole $3D + t$ domain starting from one individual marker located at a precise

[1]Resources on the synthetic embryogenetic dataset are available at http://www.die.upm.es/im/videos/TIP2012/.

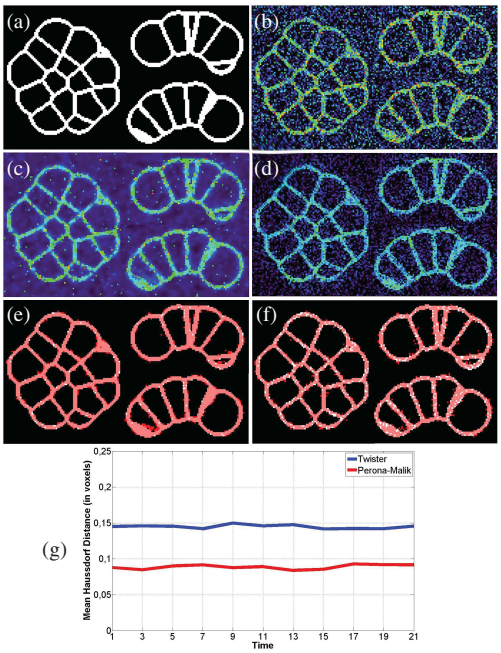

Fig. 4. Comparison of membranes filtering results. (a) Synthetic membranes used as gold standard. (b) Input to both methods: synthetic membranes with additive, uncorrelated Gaussian noise. (c) Perona–Malik filtering result. (d) Twister filtering result. (e) Final binary membranes extracted from Perona–Malik (in red) compared to the synthetic gold standard (in white). (f) Binary membranes extracted from twister filter (in red) compared to the synthetic gold standard (in white). (g) Results illustrate how the Perona–Malik and twister filters perform almost equally in terms of mean Haussdorf distance.

position in the (x, y, z, t) space. The use of a particular SE for these processes relies on the temporal interval we want to consider with respect to the marker location, e.g., time-isotropic SEs for analyzing an interval that considers future and past time points. Alternatively, causal or anti-causal time-anisotropic SEs allow to focus on one temporal direction. Nonconvex SEs (see Fig. 2) can be used to detect patterns along the temporal dimension, such as periodicity of movements i.e., we could label a planet in a particular position after every complete rotation period if we had a whole $3D+t$ sequence of its movement-. The main advantage of this processing against other tracking techniques is to use both the spatial and temporal information of each $3D + t$ object, not reducing the process to two independent processes of detection and time linking.

2) Experiments on Synthetic Data: In order to illustrate the approach, we focus on the $3D + t$ reconstruction of several cell sublineages using the unit causal hyper-cube (*forward reconstruction*), an SE that defines the 27-spatial connectivity along the current time point and the closest future one $(t, t+1)$. To generate the markers for individual cells, we detect and check the regional maxima of the first time frame. Then, the forward reconstruction with the hyper-cube is applied, highlighting connected paths referring to each marker so a cell trajectory can be isolated as an independent $3D + t$ object-. For optimal time resolution, the label of the mother cells is shared with their daughters (see Fig. 5) and then it would be possible to reconstruct any lineage branch from one marker. In some cases, because of image artifacts and low spatio-temporal resolution, the reconstruction generates false trajecto-

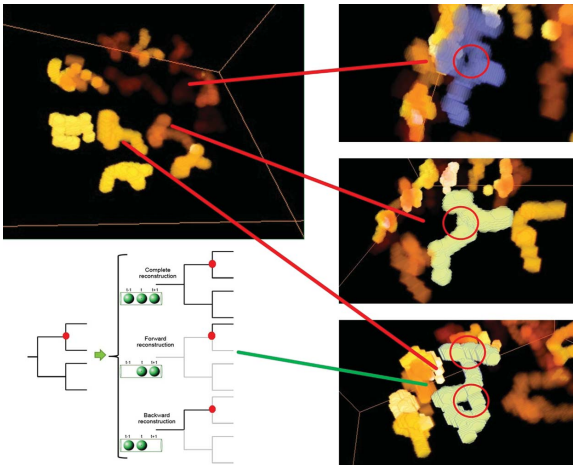

Fig. 5. 3D render of labeled nuclei trajectories after tiling all temporal frames in one volume each trajectory is one connected object. Trajectories are tubular-like structures that divide into two after mitosis. In the trajectory schema, the spatio-temporal reconstruction allows different labelization processes depending on the position of the marker and the chosen SEs. Isotropic hyper-cylinders are able to reconstruct and label all the trajectory. Causal SE track the cell forward following cell daughters in future mitosis. Anti-causal SE links the trajectory with cells ancestors.

ries, intercellular connections, and intracellular disconnections. We have done modifications on the synthetic data to observe limitations. First, data have been downsampled to be spatially isotropic $-1.04 \times 1.04 \times 1.04\ \mu\text{m}^3$ and $256 \times 256 \times 128$ voxels. A second dataset has been generated with scarcer spatial resolution $-2.08 \times 2.08 \times 2.08\ \mu\text{m}^3$ and $128 \times 128 \times 64$ voxels. For each of them, from the original temporal resolution defined by $\Delta t = 1$ min 21 s, we have time-downsampled to have lower temporal resolution $-\Delta t = 2$ min 42 s, to see the sensitivity against the timestep. To simulate a noisy acquisition, we have filtered nuclei with a Gaussian of rad $= 3$ light smoothing and other Gaussian of radius, rad $= 9$ strong smoothing resulting in two blurred versions of the original data (see Fig. 6).

Results (see Fig. 7) are obtained from comparing the resulting labeled hyper-structures with the original synthetic lineage, and expressed in terms of tracking efficiency (TE), standing for the number of good linked steps and lineage efficiency (LE), which represent the number of completely tracked lineage branches. The evaluation showed that the perfect lineage reconstruction is possible just under the optimal image characteristics, while for lower image resolutions spatial and/or temporal, even with high rates of TE ($> 90\%$), just a few hyper-structures can be completely reconstructed (LE). We have used for comparison a tracking algorithm of the ImarisTrack package of Imaris Connected components which performed worse than our method in terms of LE and TE. For light smoothing, spatial resolution 1 μm^3, and $\Delta t = 1$ m 21 s, the performance is TE $= 97\%$ and LE $= 77\%$; while for $\Delta t = 2$ min 42 s, TE $= 89\%$ and LE $= 0\%$.

Future developments should combine the morphological reconstruction with other techniques e.g., an interesting application could be to isolate each $3D+t$ trajectory and then automatically discard noisy *trajectories* using prior knowledge of possible sublineage configurations. Also, the processing

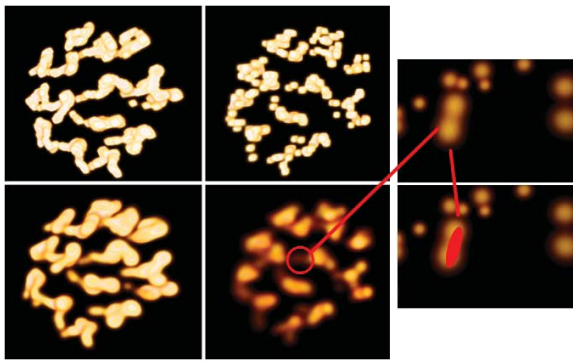

Fig. 6. Modified synthetic nuclei data with isotropic spatial resolution 2 μm^3. Left column: original temporal resolution ($1'21''$) with light smoothing (top) and strong smoothing (bottom). Center column: same renders for the t-downsampled dataset ($2'42''$). The loss of t-connectivity requires wide SEs, at the risk of connecting nuclei in their neighborhood. Right column: detail of data with low spatio-temporal resolution and strong smoothing, individual nuclei might not be distinguished inside the cell clusters.

1 µm isotropic		
	Original timestep (1'21")	Downsampled timestep (2'42")
light smoothing	TE=100% LE=100%	TE=80% LE=10%
strong smoothing	TE=95% LE=36%	TE=91% LE=36%

2 µm isotropic		
	Original timestep (1'21")	Downsampled timestep (2'42")
light smoothing	TE=95% LE=42%	TE=88% LE=21%
strong smoothing	TE=91% LE=0%	TE=82% LE=0%

Fig. 7. Summary of the morphological reconstruction tracking evaluation for the different synthetic datasets in terms of LE and TE.

do not require the consideration of more than the local context of the trajectory, thus being suitable for a parallel implementation.

D. $3D+t$ Watershed Processes

1) Spatio-Temporal Flooding Description: In the watershed segmentation method, the image is interpreted as a topographic relief altitude is given by image intensity, where each regional minimum corresponds to the source of a lake and contours of the segmentation are the dividing lines corresponding to different catchment basins once the entire relief is immersed. Watershed with markers was introduced to reduce the oversegmentation produced by flooding from all regional minima. In watershed segmentation applied to cell membrane images, a seed inside each cell is needed in order to begin the flooding process and avoid oversegmentation. The localization of all the individual markers associated to each 3D cell in the $3D+t$ domain is a hard task and certainly very difficult to validate. For this reason, an interesting application of the $3D+t$ processing, is to select cell markers just in one 3D volume (or even in a 2D slice) and extend the watershed methodology to flood directly the $3D+t$ volume (see Fig. 8). Isotropic structuring elements in space but not in time are well suited for this purpose. The hyper-sphere of radius R [see Fig. 2(f)], centered in $(x=0, y=0, z=0, t=0)$, is comprised by the voxels that verify the equation $(x^2+y^2+z^2+t^2) \leq R^2$. Along time, it corresponds to several connected spheres of increasing radius before $t=0$ and the symmetric series of

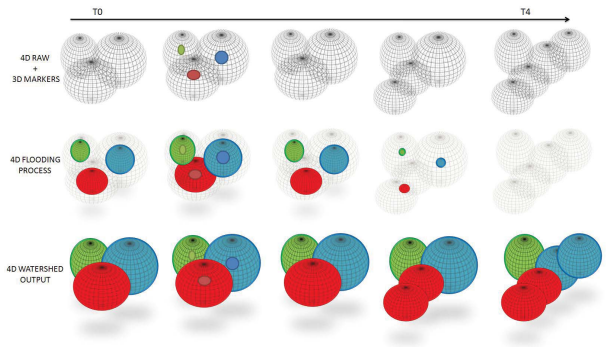

Fig. 8. Overview of $3D+t$ watershed flooding process from 3D seeds. Each single label is propagated through all the time frames producing a tracking+segmetation result.

spheres with decreasing radius toward the future. This procedure provides a coupled $3D+t$ segmentation/pseudotracking: in the context of the cell lineage, each label assigned to a cell in the 3D marker image will be propagated along the whole lineage line to which the cell belongs. This methodology is specially interesting when there is just cell membrane staining and no nuclei channel that can serve to identify the flooding seeds. Finally, spatio-temporal flooding allows to directly identify deformations of hyper-structures, such as cell membranes. In fact, there is a parallelism between the $3D+t$ flooding procedure from 3D seeds and the biological protocol of labeling cells by intracellular injection of tracer dye. Therefore, the creation of virtual cell fate maps is a straightforward application of this methodology.

2) Spatio-Temporal Viscous Operators Description: Although the standard watershed strategy is a reasonable and efficient solution for segmenting cell membranes, leakage in some poorly defined or fuzzy membrane regions, especially at low intensity levels, is a well known drawback of watershed methodology that becomes even more critical in $3D+t$. Due to low spatio-temporal resolution, spatio-temporal leakage appears producing errors in the labelization of the cell lineage besides the errors in membranes segmentation. An interesting way to enforce more spatio-temporal coherence of hyper-structures is the filtering with viscous closings/openings in $3D+t$. 3D viscous modifications of images [48] have been designed in order to smooth image contours. In a $3D+t$ context, viscous operators allow to enforce spatio-temporal connectivity and impose smoother transitions between time frames. The *oil-model fluid* is particularly interesting for the viscous closing transformation to smooth the transition of thin hyper-structures (see Fig. 9). In this model, temperature is associated to the intensity level h. Oil at low temperatures (dark pixels) has high viscosity and frontiers between regions are smoothed because fluid does not leak unless there is a space large enough to escape. At the surface level, with high temperature, oil is less viscous and watershed lines carefully follow relief like standard watershed lines do. In $3D+t$, the viscous closing transformation $T(f)$ may be implemented by adding the binary closings of image f at all the intensity levels $h>0$ with a hyper-sphere SE of radius $r(h)$, $T(f) = \vee_{h\geq 0}[\varphi_{r(h)}(h \cdot \chi_h(f))$ with $\chi_h(f)(p)=1$ for all $p \in \chi_h(f)$ and $\chi_h(f)(p)=0$ elsewhere. The function $r(h)$ defines the

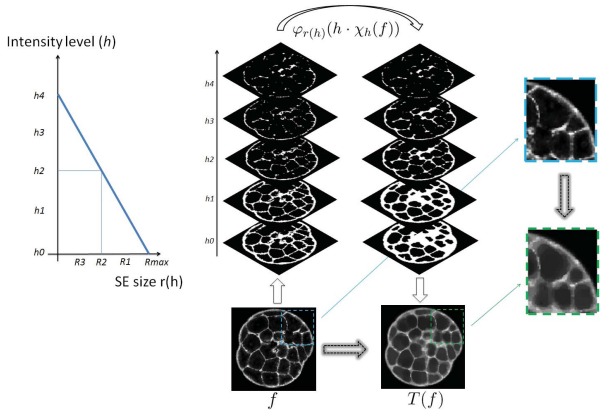

Fig. 9. Illustration of viscous closing procedure $T(f)$ in a 2D slice with five intensity levels; each of the levels is closed with a different radius.

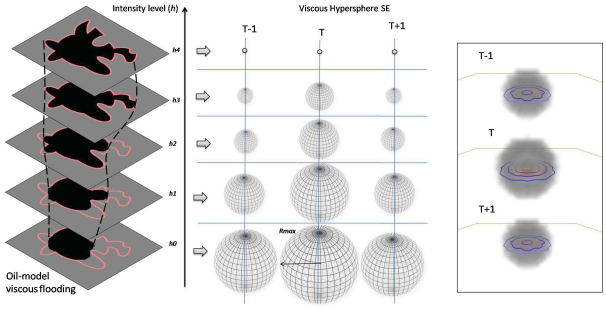

Fig. 10. Viscous hyper-sphere SE.

behavior of the fluid at different levels. The viscous closing is defined by the *oil-model* function $r(h) = R_{\max} - h * R_{\text{step}}$ performed for $r(h) > 0$ (see Fig. 10).

3) Experiments on Synthetic Data: We validate the performance of the $3D + t$ watershed approach against its 3D equivalent. As input to both methods, we use the membranes extracted by the twister filter described in Section III-B. The resulting segmentations are quantitatively evaluated for both methodologies against the gold standard provided by the synthetic dataset, in terms of volume overlap and leakage. The 3D watershed provides a very accurate cell segmentation of this synthetic data, being the main interest to assess the performance of the $3D + t$ flooding. First, to evaluate the 3D watershed, we have to manually choose the seeds from where to flood by placing one marker for each cell at each time step. This task can be very demanding when selecting markers for thousands of cells and hundreds of timesteps. On the other hand, $3D + t$ watershed only needs seeds to be specified at one frame, $t = 11$ in our case, to flood the entire spatiotemporal dataset. Then, both the standard 3D and $3D + t$ watershed algorithms are performed using a unit 3D sphere and a $3D + t$ hyper-sphere, respectively. In Fig. 11, we can note that, as segmentation propagates away from the frame where seeds are manually selected, the $3D + t$ watershed algorithm tends to perform slightly worse than its 3D equivalent in terms of leakage and overlap with respect to the gold standard. However, the $3D + t$ strategy requires much less manual interaction and its performance is still very

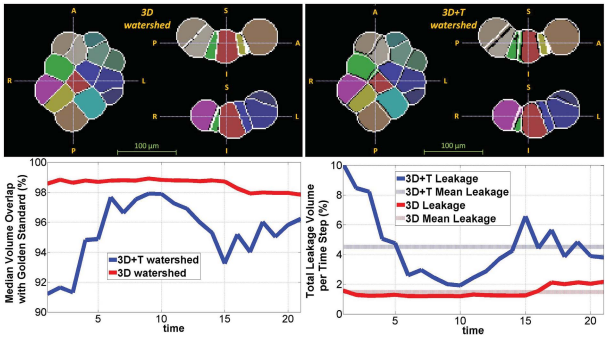

Fig. 11. 3D watershed segmentation (top left) compared to $3D+t$ (top right) at $t = 1$. This was the worst time step in terms of $3D + t$ segmentation. The graphic on the left bottom displays the median overlap, in time, of all cells with respect to their gold standard equivalents. Although 3D segmentation is better in this respects, $3D + t$ values stay always above 91%. The graphic on the right bottom displays the total % of embryo volume affected by leakage at every time point. For all timesteps, the total leakage is only 4.5% for $3D + t$ and 1.5% for the 3D approach.

reasonable (3D watershed involved a 42 min manual selection of 394 2D markers in 21 time steps. Instead, the 152-D markers employed by the $3D+t$ watershed were picked in just 2 min). An interesting future development could be a hybrid framework where an initial 4-D flooding provides the seeds to a subsequent 3D watershed that refines the final segmentation.

In order to evaluate the impact of leakage in the $3D + t$ watershed and the potential of a viscous flooding for improving the results, we introduce an artifact in the synthetic dataset by erasing all the membranes at $t = 15$. The effects of this artifact severely affect the performance of the standard 3D watershed in terms of overlap and leakage (see Fig. 12). However, the spatio-temporal closings performed by the $3D+t$ viscous flooding add more consistency to the membranes, limiting the effects of the temporal spill. The parameters chosen in this case for the *oil-model* flooding are $R_{\text{step}} = 1$ pixel, $h_v = 255$ gray level, and $R_{\max} = 3$ pixels used for a hyper-sphere SE limited to $t + 1$ and $t - 1$.

E. $3D + t$ Skeletonization

1) Description: Skeletonization [49] is a widely used transformation that simplifies a $N + 1$ dimensional binary object into a N dimensional object that preserves its topology. There are many kinds of skeletonization techniques that have been successfully applied in 2D and 3D. However, the use of skeletons in 4-D is much less expanded, and few real applications have been proposed, i.e., planning of collision free routes for multiple vehicles [50]. An integrated $3D + t$ skeleton, gives information about the trace of an object moving on time and its topology. Among the various theoretical approaches for calculating a spatio-temoral skeleton [51], we have chosen to implement a skeletonization algorithm based on the *hit-or-miss* transformation and shape primitives presented in [50]. Thinning methodologies preserve the homotopy of the object, so that the skeleton has the same number of connected elements as the initial binary gene expression image. The hit-or-miss transformation is defined as: $\varepsilon_{B1}(f) \bigcap \varepsilon_{B2}(\bar{f})$ (where ε is the erosion operator). It preserves pixels whose neighborhood matches the shape of structuring element $B1$ but

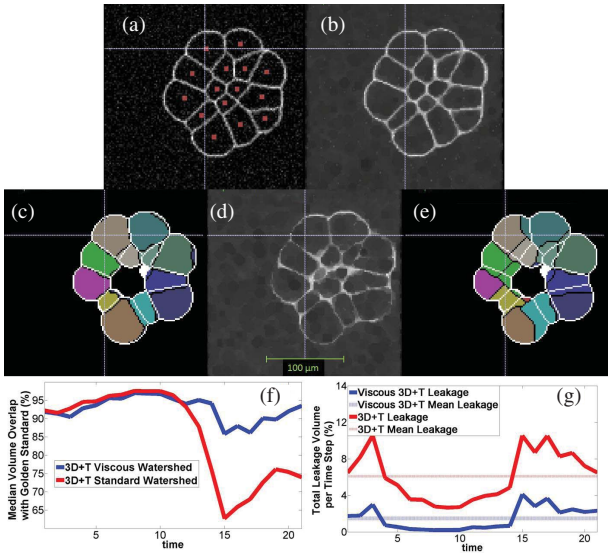

Fig. 12. (a) Transversal view of the membranes and the 2D seeds used to flood at $t = 11$. (b) Membranes at $t = 11$ after viscous closing. (c) Membranes reconstructed by the spatio-temporal viscous closing at $t = 15$, the time frame where membranes were initially erased. (d) and (e) Comparisons between the gold standard (in white) and the cell segmentations achieved at $t = 15$ by the viscous and the standard $3D+t$ watersheds, respectively. (f) Median overlap, in %, between the segmented cells in every time step with respect to their gold standard equivalents. (g) Total % of the embryo volume affected by leakage at every time point. For both overlap and leakage, we can appreciate how the $3D + t$ viscous watershed drastically improves the performance of the standard method.

not the shape of $B2$. $3D + t$ skeletons might be an efficient way to reduce data dimensionality and characterize gene expression data, thus allowing to capture the dynamics and topology of gene patterns in real images of morphogenesis (see Section IV-E).

IV. Experiments With *In-Vivo* $3D + t$ Zebrafish Embryogenesis Data

A. Membranes Filtering by Twister Hyper-Segment

1) Dataset and Experiment Description: The twister filtering using hyper-segment structuring elements has been applied to data from a live zebrafish embryo featuring cell membranes marked through the expression of a red fluorescent protein. These images have been acquired with a two-photon LSM. Image size is $512 \times 512 \times 60$ and voxel size is $0.58 \times 0.58 \times 1\ \mu\text{m}^3$. Images were acquired with $\Delta t = 5$ min for several hours starting at 3.5 hours of development at 28 °C. In this example, the size of the line segment has been adjusted manually to seven pixels. The SE has been cropped in the time axis, so the line segments of the twister structuring element are embedded in a $3D+t$ box of size $(x = 7, y = 7, z = 7, t = 3)$. In order to avoid abrupt intensity variations, the output is smoothed by a spherical averaging filter of two pixels radius. Cross sections of original and filtered images are shown in Fig. 13.

2) Results Discussion: Visual inspection of results attest that the proposed method efficiently removes noise and that the quality of the filtering is, at least, comparable to the 3D Perona–Malik. More generally, the twister SEs might be of great interest to filter and label hyper-structures in a quite

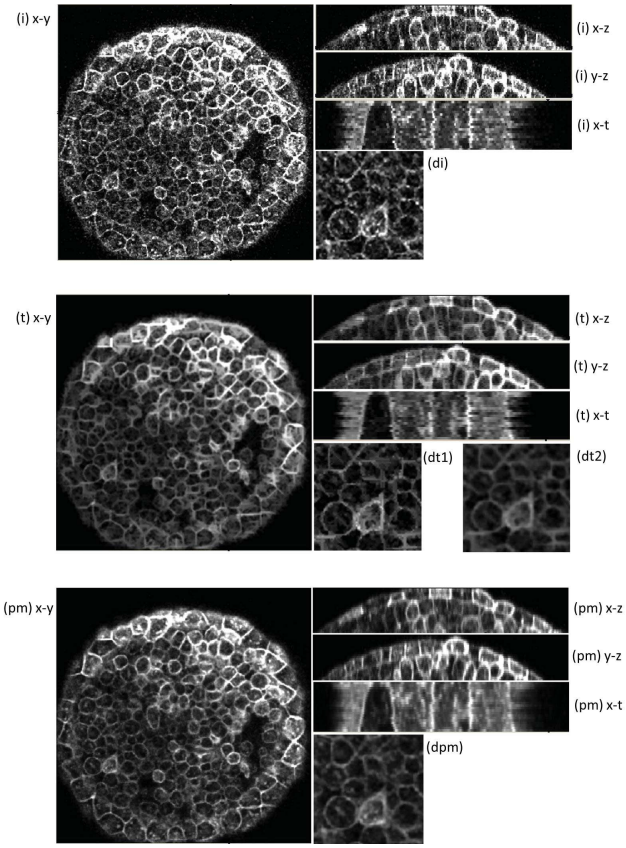

Fig. 13. Results of twister segment filtering. i: Cross sections of the original image. pm: Cross sections of the image filtered by Perona-Malik 3D anisotropic diffusion filter (*ITK* method *[itk::GradientAnisotropicDiffusionImageFilter]* with parameters $iter = 5$, $t = 0.625$ and $k = 100$). t: Cross sections of the image filtered by the twister segment opening and regularized with a circular averaging. di: Detail of the x-y cross section of the original image. dpm: Detail of the image filtered by the Perona–Malik filter. dt1: Detail of the image opened with the twister structuring element. dt2: Detail of dt1 after circular averaging filter.

generic way, e.g., when cells differentiate and begin to build interesting structures by aligning their membranes and moving persistently in given directions due to mechanical factors.

B. Cell Nuclei Tracking in Fluorescence Images

1) Dataset and Experiment Description: The $3D + t$ morphological reconstruction has been applied to cell back-tracking using anti-causal hyper-cylinders, characterized by an spatial isotropic radius R, and a temporal radius T HC(R, T) [see Fig. 2(d)]. It has been validated in a cell nuclei dataset (marked with a GFP) acquired with a two-photon LSM over a zebrafish embryo, during its early development for 2 h with $\Delta t = 30$ s and spatial resolution $1.09 \times 1.09 \times 2.18\ \mu\text{m}^3$. Image dataset has been preprocessed with a diffusion filter [13] and a morphological 3D area filtering [42] to smooth nuclei regions. The method is triggered from initial markers selected after generating a gold standard reference for 20 trajectories manually. For validation, we have reconstructed the trajectories along 120 time steps, with different temporal resolutions $\Delta t = 30$ s, $\Delta t = 60$ s, $\Delta t = 120$ s and using several temporally anisotropic HCs. These tests aim at

		HC(1,1)	HC(1,2)
Δt=30"	TE /LE (%)	99,54 / 70	99,75 / 80
Δt=60"	TE /LE (%)	98,50 / 70	99,67 / 75
Δt=120"	TE /LE (%)	98,95 / 65	-

Fig. 14. Performance results (tracking efficiency and lineage Efficiency) of the hyper-tubes HC(1, 1) and HC(1, 2) applied to images sequences with increasing time step.

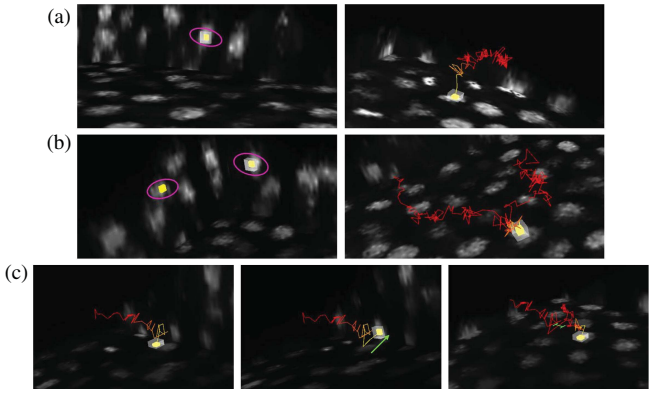

Fig. 15. Tracking examples of (a) single-cell trajectory and (b) dividing cell. (c) Example of tracking failure resulting in a "switch" between cells. All cases were reconstructed with HC(1, 2) and $\Delta t = 30$ s.

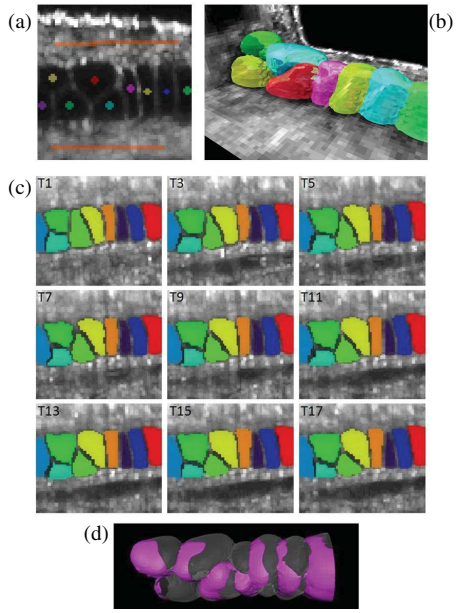

Fig. 16. (a) Watershed seeds superimposed to raw data. (b) Volume rendering of membranes segmentation at $T = 9$. (c) Evolution of membrane shapes from $T = 1$ to $T = 17$. (d) Volume rendering of segmentations: $T = 1$ in gray and $T = 17$ in purple.

giving more clues about the exploitation of spatio-temporal integration of $3D + t$ operators and their sensitivity in this data domain. For evaluating performance, we use the LE and TE as in the synthetic data experiments (see Fig. 14).

2) Results Discussion: The causal hyper-cylinder HC$(1, 1), t \leq 0$, which features the minimum spatio-temporal connectivity to reconstruct backwards, obtains high TE rates, but the small miss rate produces not so good LE. Tracking errors are due to SNR and the image artifacts of acquisition. In order to prevent this, we tested HC$(1, 2), t \leq 0$ (longer T) which makes the reconstruction *more robust against intensity variations* in time. Consistently, the results show that this SE improves both metrics. Then, we applied these HCs to the $\Delta t = 60$ s sequence obtaining fairly similar results. For $\Delta t = 120$ s, both TE and SE are less satisfactory as the shifts during mitosis cannot be connected. We also tested HC(3, 1) (longer R) for $\Delta t = 60$ s to connect longer displacements, but the results LE 30%, TE 97.08% are poor as enlarging the spatial radius makes the reconstruction interconnect neighbors. Overall, in these conditions, the proposed methodology allows reconstructing a cell trajectory from a single marker when $\Delta t \leq 60$ s [see Fig. 15(a) and (b)]. This conclusion reinforces the idea that, for each particular dataset, there is a limit spatio-temporal resolution for which the algorithm works, that strongly depends on the data and the topology of the 4-D objects.

C. Somite Cell Segmentation in Zebrafish Tail with Standard $3D + t$ Watershed

1) Dataset and Experiment Description: Images from zebrafish tail at 36 hours post fertilization (hpf) have been acquired with LSFM microscopy. A volume of $75 \times 75 \times 75 \times 18$ voxels with isotropic resolution of 1.5 μm and $\Delta t = 300$ s containing nine somite cells has been selected for segmentation. The somites are characteristic cells arranged along the dorsoventral axis of zebrafish that develop into serial blocks comprised of muscle, cartilage, and bone which are typical from vertebrates precursors from human backbone. In order to initialize the $3D + t$ watershed flooding, seeds have been manually located inside nine cells at time step 9 (note that markers have been placed into a 2D slice in less than 1 min). Two markers have also been added for segmenting the outside region of somites. In order to enhance gradients in the membranes image, the internal morphological gradient $(f - \varepsilon_B(f))$ has been added to the original image. Then, the standard watershed transformation has been executed using the manually selected markers and a unit hyper-sphere $HS(1)$ [see Fig. 2(f)].

2) Results Discussion: Results have been visually validated, showing a correct segmentation of the $3D+t$ shapes associated to each of the nine somite cells along the whole hyper-volume 18 time points (see Fig. 16). This simple experiment illustrates the benefits of this methodology: it saves time while selecting markers for segmentation and provides a spatio-temporal coherent "tracking" of cell membrane shapes that evolve smoothly in $3D + t$.

D. Fate Maps in Early Zebrafish Embryogenesis Using $3D+t$ Viscous Watershed Flooding

1) Dataset and Experiment Description: Third harmonic generation (THG) [8] microscopy of unstained zebrafish embryo provides a high-quality view of cell membrane morphology during the first hours of embryogenesis. In the following experiment, we illustrate the spatio-temporal segmentation of cell membranes from a THG sequence where data are likely to produce spatio-temporal leakage (Fig. 17). The goal of this experiment is to obtain the cell fate maps of the first 16 cells into the 128 cells stage performing a $3D + t$

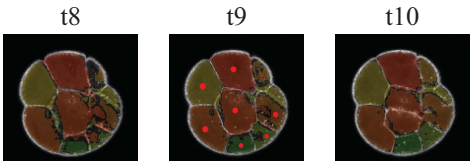

Fig. 17. Example of $3D+t$ standard watershed. Cross sections of three consecutive volumes. Seeds are located in $t9$ (red dots). Different labels overimposed to raw data correspond to segmented $3D+t$ cells. Segmentations are not accurate: white lines corresponding to membranes in the raw data do not overlap with frontiers between labels because of spatio-temporal leakage.

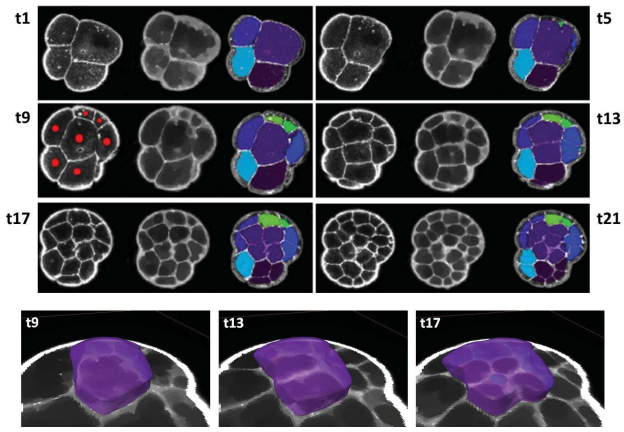

Fig. 18. 4-D viscous watershed segmentation of epithelial cells: cross sections of raw data (left), viscous closing (middle), and output of $3D+t$ viscous watershed process for time steps 1, 5, 9, 13, 17, and 21. Seeds are signaled in red at $t9$. Each cell lineage is labeled with the same label generated in the frame with the markers.

flooding process over a 20 time points dataset ($\Delta t = 228$ s). Watershed seeds at the 16 cells stage have been manually added. This task is very complex for automated cell tracking methods as synchronized mitosis usually lead to errors in the lineage generation.

2) Results Discussion: We have applied the described spatio-temporal viscous flooding for the watershed segmentation so that the leakage can be avoided. The *oil-model* flooding parameters $R_{\max}$, R_{step}, and T have been chosen empirically (see Fig. 9). Tests showed that the best results are achieved when $R_{\max}$ is around 6 times smaller than the estimated mean cell radius at the corresponding cell cycle and R_{step} has a fixed value related to the level $h_v = R_{\max}/R_{\text{step}}$ from where viscosity effects are neglected (h_v is the intensity maximum of the THG signal). T is just 1 to force spatio-temporal smoothness, so the viscous dilation of each point at time t affects volumes at $t-1$ and $t+1$. Results on these data have been visually validated showing that leakage problems are solved in most of the cases, when the label propagation arrives inside the 3D volume of the cell in the following time step, it does not flood other cells. In case of mitosis, the flooding will propagate the label to both daughters if the overall envelope of both daughters is similar to the membrane of the mother. This phenomenon poses a more restrictive requirement for the temporal resolution as the joint envelope of both daughter cells will differ for the membrane of the cell mother at about 5 min at this developmental stage. The 16 cells ($3D+t$ structures) can be divided into two groups: 12 epithelial cells and four internal cells that stand between the yolk (an inner mass of nutrients under the cells). The $3D+t$ shape of eight epithelial cells has been correctly segmented (see Fig. 18), while the remaining four epithelial cells fate maps are just partially segmented because the background marker leaked in the interface with the yolk producing uncomplete fate maps. Segmentation results on the four internal cells were incorrect from the beginning. Thus, this methodology is not well suited for segmenting the internal cells of zebrafish early development because of the interface with yolk, which is not clearly defined and has a fast movement that produces a membrane displacement from frame to frame, which cannot be *connected* by the viscous closing and it would require manual delimitation of the yolk (see Fig. 19). Overall, spatio-temporal viscous operators enforce the spatio-temporal consistency of segmented hyper-surfaces by smoothing the flooding process and reducing temporal leakage. On the other hand, viscous flooding needs an heuristic parameter choice dependent on the image characteristics (in contrast to the parameter-free standard watershed).

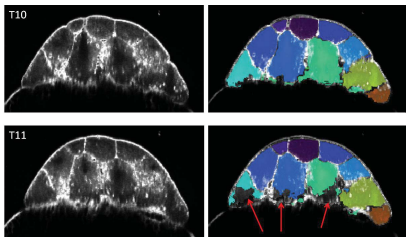

Fig. 19. Red arrows point temporal leakage problems when dealing with cells touching the interface with the yolk as the cell contours have much poorer spatial resolution there.

E. Topological Description of Spatio-Temporal Gene Expression

1) Dataset and Experiment Description: Understanding morphogenetic processes during development requires capturing quantitative data of gene expression in time and space at cellular scale [52]. In this context, we apply the presented spatio-temporal skeleton approach to characterize the $3D+t$ *shape* of the regions expressing a certain gene. Concretely, we have analyzed an image dataset of a transgenic fish line expressing the goosecoid (*gsc*) gene acquired with two-photon LSM during the gastrulation period between 6 and 9 hpf. During this period, the transcriptional factor we focused on, *gsc*, starts its expression at the dorsal side to later on move up to the animal pole giving birth to the dorsal axis. The image data size after downsampling is $128 \times 128 \times 62 \times 100$ with an isotropic spatial resolution of 6 μm and $\Delta t = 1$ min 50 s. Embryo regions showing gene expression have high image intensity values, thus image has been thresholded in order to obtain the binary mask retaining the $3D+t$ shape (see Fig. 20).

2) Results Discussion: The resulting skeleton is a 3D volume embedded in the $3D+t$ space that shows *gsc* gene expression migrating during gastrulation and dividing symmetrically into two region during eye formation. *Collapsing* this $3D+t$ space along the temporal dimension into one 3D volume provides a simple method to understand gene expression

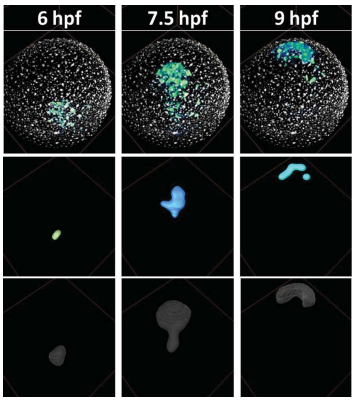

Fig. 20. Top row: view from the animal pole showing the nuclei and *gsc* expression of the imaged zebrafish at 6, 7.5, and 9 hpf. Middle row: resulting skeleton of the *gsc* domain. Bottom row: binary mask of the *gsc* domain used for the skeletonization.

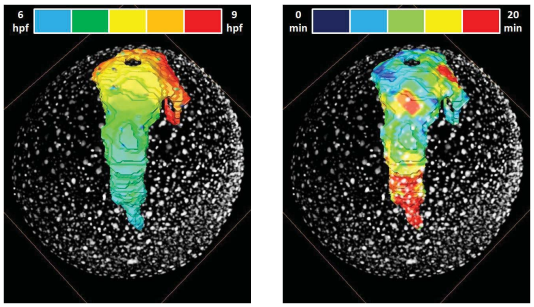

Fig. 21. Left: the skeleton offers a representation of the temporal moments when the *gsc* was last expressed on the 3D volume. Right: the skeleton offers a representation of the endurance of *gsc* expression on the 3D volume. Note: in order to contextualize the spatial position, the skeletons have been overimposed to a 3D rendering of cell nuclei at *7.5 hpf*.

dynamics. For instance, taking the maximum value over t in each (x, y, z) position of the $3D + t$ skeleton, allows to quantify when the gene expression was last expressed in each particular point. Another way of interpreting the *collapsed* skeleton is adding all the binary $3D + t$ frames into one 3D volume, allowing to see the persistence of the gene expression in each spatial position (see Fig. 21). This illustrative example shows how skeletonization can be used to characterize the spatio-temporal hyper-shape of gene expression data during zebrafish development. This kind of representation can be used in future works to compare different gene expression hyper-shapes or characterize the $3D+t$ topology of gene expression.

V. Conclusion

A. Summary

This research defined the spatio-temporal structuring elements required to process $3D + t$ data with morphological operators and classified them according to their isotropy and convexity in both the spatial and temporal dimensions. The main idea when operating directly in the $3D + t$ domain is that moving objects can be treated as single entities (*hyper-structures*) e.g., cells as tree-like $3D + t$ tubes. In order to illustrate the potential applications to *in-vivo* embryogenesis image analysis, we have created a synthetic embryogenetic dataset used to test and validate four representative methods[2] that worked directly in the $3D + t$ space. The methods have also been applied to microscopy data of *in-vivo* zebrafish embryogenesis and can be summarized as follows.

1) Denoising cell membrane images with the twister segment filtering, a multidimensional extension of the morphological filtering based on openings by line segments.
2) Cell tracking based on the morphological reconstruction by dilation, starting from a nuclei marker and identifying the cell trajectory as a single 4-D object.
3) Generation of virtual cell fate maps with standard and viscous $3D + t$ watershed from seeds in one 3D frame.
4) Skeletonizaton of spatio-temporal topologies to simplify and quantify gene expression domains.

B. Discussion and Perspectives

Overall, the main advantage of analyzing directly $3D + t$ images comes from the inherent redundancy of the temporal dimension. Why analyze 3D volumes separately if we are looking for 4-D patterns?

The proposed methodology is a conceptual extension that sets up a common flexible framework to apply morphological operators and exploits both temporal and spatial features of $3D + t$ images. *In-vivo* images of embryogenesis are an appropriate benchmark as they feature large number of structures with characteristic spatio-temporal properties, such as cell displacements and deformations. The benefits of this kind of processing in terms of coherence and efficiency are dependent on the particular application. In some cases, this approach allows faster analysis, as the whole volume is processed directly and it does not require recursive or iterative algorithms. In other cases, the spatio-temporal local context will provide enough information so the processing can be parallelized using few markers as seeds for the operators. Another effective strategy is that each 4-D object can be isolated, visualized, and analyzed individually, helping to scale the validation process of large amounts of data. This is a major motivation: usually in approaches where 3D segmentations are followed by a global tracking that link objects *a posteriori*, the time required for validation is huge. The major limitation of the 4-D approach is therefore the sensitivity against the spatio-temporal resolution: changing the acquisition sampling rate might change the spatio-temporal shape of the analyzed objects ($3D + t$ hyper-structures). However, future advances in imaging techniques will only provide better resolutions. The proposed methods are just illustrative and we expect them to serve as basis and inspiration for new strategies that can use the proposed structuring elements. Future research lines include the generation of hybrid frameworks where initial $3D + t$ processing is refined later by more accurate 3D methods. Another interesting potential development is the use

[2]All these methods have been prototyped in MATLAB using the *Image Processing Toolbox* and the *SDC Morphology Toolbox*. Some of the methods have also been implemented in C++ using the *Insight ToolKit (ITK)* framework and the mathematical morphology contributions to the framework [53], [54].

of spatiotemporally-variant structuring elements, that in the case of embryogenesis imaging, might be driven by vector field computations of cell or tissue deformations.

ACKNOWLEDGMENT

The authors would like to thank the ccIN2P3, J.-Y. Nief and P. Calvat for their support with data management, I. Colin, S. Desnoulez, and A. Colin for their excellent technical assistance, P. Parra and J.-Y. Tiercelin for precision mechanics, and E. Beaurepaire for the third harmonic generation image datasets.

REFERENCES

[1] A. Abbott, "Microscopic marvels: Seeing the system," *Nature*, vol. 459, no. 7247, pp. 630–631, 2009.

[2] A. Oates, N. Gorfinkiel, M. González-Gaitán, and C.-P. Heisenberg, "Quantitative approaches in developmental biology," *Nature Rev. Genet.*, vol. 10, no. 8, pp. 517–530, 2009.

[3] M. A. Luengo-Oroz, M. J. Ledesma-Carbayo, N. Peyriéras, and A. Santos, "Image analysis for understanding embryo development: A bridge from microscopy to biological insights," *Current Opinion Genet. Develop.*, vol. 21, no. 5, pp. 630–637, Sep. 2011.

[4] C. Kimmel, W. W. Ballard, S. R. Kimmel, B. Ullmann, and T. F. Schilling, "Stages of embryonic development of the zebrafish," *Develop. Dyn.*, vol. 203, no. 3, pp. 253–310, 1995.

[5] J. Amatruda, J. L. Shepard, H. M. Stern, and L. I. Zon, "Zebrafish as a cancer model system," *Cancer Cell*, vol. 1, no. 3, pp. 229–231, 2002.

[6] S. Megason and S. E. Fraser, "Digitizing life at the level of the cell: High-performance laser-scanning microscopy and image analysis for in toto imaging of development," *Mech. Develop.*, vol. 120, no. 11, pp. 1407–1420, 2003.

[7] P. Keller, A. D. Schmidt, J. Wittbrodt, and E. H. K. Stelzer, "Reconstruction of zebrafish early embryonic development by scanned light sheet microscopy," *Science*, vol. 322, no. 5904, pp. 1065–1069, 2008.

[8] N. Olivier, M. A. Luengo-Oroz, L. Duloquin, E. Faure, T. Savy, I. Veilleux, X. Solinas, D. Débarre, P. Bourgine, A. Santos, N. Peyriéras, and E. Beaurepaire, "Cell lineage reconstruction of early zebrafish embryos using label-free nonlinear microscopy," *Science*, vol. 329, no. 5994, pp. 967–971, Aug. 2010.

[9] M. A. Luengo-Oroz, J. L. Rubio-Guivernau, E. Faure, T. Savy, L. Duloquin, N. Olivier, D. Pastor, M. Ledesma-Carbayo, D. Débarre, P. Bourgine, E. Beaurepaire, N. Peyriéras, and A. Santos, "Methodology for reconstructing early zebrafish development from in vivo multiphoton microscopy," *IEEE Trans. Image Process.*, vol. 21, no. 4, pp. 2335–2340, Apr. 2012.

[10] W. Denk and J. H. Strickler, "Two-photon laser scanning fluorescence microscopy," *Science*, vol. 248, no. 4951, pp. 73–76, 1990.

[11] C. K. Sun, S. W. Chu, S. Y. Chen, T. H. Tsai, T. M. Liu, C. Y. Lin, and H. J. Tsai, "Higher harmonic generation microscopy for developmental biology," *J. Struct. Biol.*, vol. 147, no. 1, pp. 19–30, 2004.

[12] E. Meijering, I. Smal, and G. Danuser, "Tracking in molecular bioimaging," *IEEE Signal Process. Mag.*, vol. 23, no. 3, pp. 46–53, May 2006.

[13] Z. Krivá, K. Mikula, N. Peyriéras, B. Rizzi, A. Sarti, and O. Stasová, "3-D early embryogenesis image filtering by nonlinear partial differential equations," *Med. Image Anal.*, vol. 14, no. 4, pp. 510–526, Apr. 2010.

[14] J. B. de Monvel, S. L. Calvez, and M. Ulfendahl, "Image restoration for confocal microscopy: Improving the limits of deconvolution, with application to the visualization of the mammalian hearing organ," *Biophys. J.*, vol. 80, no. 5, pp. 2455–2470, 2001.

[15] T. Chuang, S. Moshir, Y. Garini, A. Y.-C. Chuang, I. T. Young, B. Vermolen, R. Doel, V. Mougey, M. Perrin, M. Braun, P. D. Kerr, T. Fest, P. Boukamp, and S. Mai, "The three-dimensional organization of telomeres in the nucleus of mammalian cells," *BMC Biol.*, vol. 2, pp. 12–24, Jun. 2004.

[16] J. Olivo-Marin, "Extraction of spots in biological images using multiscale products," *Pattern Recognit.*, vol. 35, no. 9, pp. 1989–1996, Sep. 2002.

[17] P. Frolkovic, K. Mikula, N. Peyriéras, and A. Sarti, "Counting number of cells and cell segmentation using advection-diffusion equations," *Kybernetika-Praha*, vol. 43, no. 6, pp. 817–829, 2007.

[18] C. Zimmer, Z. Bo, A. Dufour, A. Thebaud, S. Berlemont, V. Meas-Yedid, and J.-C. O. Marin, "On the digital trail of mobile cells," *IEEE Signal Process. Mag.*, vol. 23, no. 3, pp. 54–62, May 2006.

[19] C. Melani, M. Campana, B. Lombardot, B. Rizzi, F. Veronesi, C. Zanella, P. Bourgine, K. Mikula, N. Peyriéras, and A. Sarti, "Cells tracking in a live zebrafish embryo," in *Proc. 29th IEEE Annu. Int. Conf. Eng. Med. Biol. Soc.*, Aug. 2007, pp. 1631–1634.

[20] A. Dufour, V. Shinin, S. Tajbakhsh, N. Guillen-Aghion, J. C. Olivo-Marin, and C. Zimmer, "Segmenting and tracking fluorescent cells in dynamic 3-D microscopy with coupled active surfaces," *IEEE Trans. Image Process.*, vol. 14, no. 9, pp. 1396–1410, Sep. 2005.

[21] C. Zimmer, E. Labruyere, V. Meas-Yedid, N. Guillen, and J.-C. Olivo-Marin, "Segmentation and tracking of migrating cells in videomicroscopy with parametric active contours: A tool for cell-based drug testing," *IEEE Trans. Med. Imag.*, vol. 21, no. 10, pp. 1212–1221, Oct. 2002.

[22] E. Meijering, M. Jacob, J. C. Sarria, P. Steiner, H. Hirling, and M. Unser, "Design and validation of a tool for neurite tracing and analysis in fluorescence microscopy images," *Cytometry A*, vol. 58, no. 2, pp. 167–176, 2004.

[23] C. Zanella, M. Campana, B. Rizzi, C. Melani, G. Sanguinetti, P. Bourgine, K. Mikula, N. Peyrieras, and A. Sarti, "Cells segmentation from 3-D confocal images of early zebrafish embryogenesis," *IEEE Trans. Image Process.*, vol. 19, no. 3, pp. 770–781, Mar. 2010.

[24] P. Kramer, F. Boto, D. Wald, F. Bessy, C. Paloc, C. Callol, A. Letamendia, I. Ibarbia, O. Holgado, and J. M. Virto, "Comparison of segmentation algorithms for the zebrafish heart in fluorescent microscopy images," in *Proc. 5th Int. Symp. Adv. Vis. Comput. II*, 2009, pp. 1041–1050.

[25] F. de Chaumont, S. Dallongeville, and J.-C. Olivo-Marin, "Icy: A new open-source community image processing software," in *Proc. 8th IEEE Int. Symp. Biomed. Imag.*, Mar.–Apr. 2011, pp. 234–237.

[26] W. Supatto, A. McMahon, S. E. Fraser, and A. Stathopoulos, "Quantitative imaging of collective cell migration during drosophila gastrulation: Multiphoton microscopy and computational analysis," *Nature Protocols*, vol. 4, no. 10, pp. 1397–1412, 2009.

[27] S. Bonneau, M. Dahan, and L. D. Cohen, "Single quantum dot tracking based on perceptual grouping using minimal paths in a spatiotemporal volume," *IEEE Trans. Image Process.*, vol. 14, no. 9, pp. 1384–1395, Sep. 2005.

[28] A. Abufadel, T. Yezzi, and R. W. Schafer, "4-D segmentation of cardiac data using active surfaces with spatiotemporal shape priors," *Appl. Pattern Recognit.*, vol. 91, pp. 77–100, Jan. 2008.

[29] J. Montagnat and H. Delingette, "4-D deformable models with temporal constraints: Application to 4-D cardiac image segmentation," *Med. Image Anal.*, vol. 9, no. 1, pp. 87–100, 2005.

[30] D. Mischler, B. Romaniuk, A. Benassarou, and E. Bittar, "Robust 4-D segmentation of cells in confocal images," in *Proc. Int. Conf. Comput. Vis. Graph.*, 2006, pp. 1–6.

[31] M. Luengo-Oroz, E. Faure, B. Lombardot, R. Sance, P. Bourgine, N. Peyriéras, and A. Santos, "Twister segment morphological filtering. A new method for live zebrafish embryos confocal images processing," in *Proc. IEEE Int. Conf. Image Process.*, vol. 5. Sep.–Oct. 2007, pp. 253–256.

[32] D. Pastor, M. A. Luengo-Oroz, B. Lombardot, I. Gonzalvez, L. Duloquin, T. Savy, P. Bourgine, N. Peyrieras, and A. Santos, "Cell tracking in fluorescence images of embryogenesis processes with morphological reconstruction by 4D-tubular structuring elements," in *Proc. IEEE Int. Conf. Eng. Med. Biol. Soc.*, Sep. 2009, pp. 970–973.

[33] F. Meyer, "Iterative image transformations for an automatic screening of cervical smears," *J. Histochem. Cytochem.*, vol. 27, no. 1, pp. 128–135, 1979.

[34] J. Angulo and S. Matou, "Application of mathematical morphology to the quantification of in vitro endothelial cell organization into tubular-like structures," *Cellular Molecular Biol.*, vol. 53, no. 2, pp. 22–35, 2007.

[35] M. Luengo-Oroz and J. Angulo, "Cyclic mathematical morphology in polar-logarithmic representation," *IEEE Trans. Image Process.*, vol. 18, no. 5, pp. 1090–1096, May 2009.

[36] G. Lin, U. Adiga, K. Olson, J. F. Guzowski, C. A. Barnes, and B. Roysam, "A hybrid 3-D watershed algorithm incorporating gradient cues and object models for automatic segmentation of nuclei in confocal image stacks," *Cytometry A*, vol. 56, no. 1, pp. 23–36, 2003.

[37] A. Vincent, R. Christian, and H. Fabrice, "Spatio-temporal segmentation using 3-D morphological tools," in *Proc. Int. Conf. Pattern Recognit.*, 2000, pp. 3885–3892.

[38] L. Marak, J. Cousty, L. Najman, and H. Talbot. (2009). 4-D morphological segmentation and the MICCAI LV-segmentation grand challenge. *MIDAS J.* [Online]. Available: http://hdl.handle.net/10380/3085
[39] W. Higgins and J. Lee, "4D morphological processing of cardiac image sequences," in *Proc. IEEE 15th Annu. Int. Conf. Eng. Med. Biol. Soc.*, pp. 136–137, Oct. 1993,
[40] J. Serra, *Image Analysis and Mathematical Morphology*. San Francisco, CA: Academic, 1983.
[41] M. Luengo-Oroz, L. Duloquin, C. Castro, T. Savy, E. Faure, B. Lombardot, R. Bourgine, N. Peyrieras, and A. Santos, "Can voronoi diagram model cell geometries in early sea-urchin embryogenesis?" in *Proc. 5th IEEE Int. Symp. Biomed. Image Nano Macro*, May 2008, pp. 504–507.
[42] L. Vincent, "Morphological area opening and closing for grayscale images," in *Shape in Picture Workshop*. New York: Springer-Verlag, 1992, pp. 197–208.
[43] C. L. L. Hendriks and L. J. van Vliet, "Using line segments as structuring elements for sampling-invariant measurements," *IEEE Trans. Pattern Anal. Mach. Intell.*, vol. 27, no. 11, pp. 1826–1831, Nov. 2005.
[44] P. Perona and J. Malik, "Scale-space and edge detection using anisotropic diffusion," *IEEE Trans. Pattern Anal.*, vol. 12, no. 7, pp. 629–639, Jul. 1990.
[45] G. Gerig, O. Kubler, R. Kikinis, and F. A. Jolesz, "Nonlinear anisotropic filtering of MRI data," *IEEE Trans. Med. Imag.*, vol. 11, no. 2, pp. 221–232, Jun. 1992.
[46] S. Pop, A. Dufour, and J.-C. Olivo-Marin, "Image filtering using anisotropic structure tensor for cell membrane enhancement in 3-D microscopy," in *Proc. 18th IEEE Int. Conf. Image Process.*, Sep. 2011, pp. 2041–2044.
[47] L. Vincent, "Morphological grayscale reconstruction in image analysis: Applications and efficient algorithms," *IEEE Trans. Image Process.*, vol. 2, no. 2, pp. 176–201, Apr. 1993.
[48] C. Vachier and F. Meyer, "The viscous watershed transform," *J. Math. Image Vis.*, vol. 22, nos. 2–3, pp. 251–267, 2005.
[49] H. Blum, "A transformation for extracting new descriptors of shape," *Models Percept. Speech Vis.*, vol. 19, no. 5, pp. 362–380, 1967.
[50] P. Jonker, "Morphological operations on 3-D and 4-D images: From shape primitive detection to skeletonization," in *Discrete Geometry for Computer Imagery*. New York: Springer-Verlag, 2000, pp. 371–391.
[51] L. Vincent, "Efficient computation of various types of skeletons," *Proc. SPIE Med. Imag. V*, vol. 1445, pp. 297–311, Feb. 1991.
[52] C. Castro, M. A. Luengo-Oroz, S. Desnoulez, L. Duloquin, L. Fernandez-de-Manuel, S. Montagna, M. J. Ledesma-Carbayo, P. Bourgine, N. Peyrieras, and A. Santos, "An automatic quantification and registration strategy to create a gene expression atlas of zebrafish embryogenesis," in *Proc. IEEE Int. Conf. Eng. Med. Biol. Soc.*, vol. 1. Sep. 2009, pp. 1469–1472.
[53] G. Lehmann. (2008). Label object representation and manipulation with ITK. *Insight J.* [Online]. Available: http://hdl.handle.net/1926/584
[54] R. Beare. (2007). Grayscale morphological attribute operations. *Insight J.* [Online]. Available: http://hdl.handle.net/1926/1316

Miguel A. Luengo-Oroz received the Ph.D. and M.S. degrees in telecommunications engineering from Universidad Politécnica de Madrid (UPM), Madrid, Spain, and the M.S. degree in cognitive science from l'École des Hautes Etudes en Sciences Sociales, Paris, France.

He has been a Visiting Researcher with l'École Polytechnique, Complex Systems Institute of Paris and l'École des Mines de Paris. He was a Lead Data Specialist with United Nations, New York, NY, in 2011. He is currently a Research Scientist with the Biomedical Image Technologies Group, UPM. His current research interests include pattern recognition, quantitative analysis, and complex systems applied to biomedicine and human development.

David Pastor-Escuredo received the M.S. degree in electrical engineering and computer science from Universidad Politécnica de Madrid (UPM), Madrid, Spain, in 2008. He is currently pursuing the Ph.D. degree with Biomedical Image Technologies Group, UPM.

His current research interests include the reconstruction of multiscale dynamics in living systems morphogenesis.

Carlos Castro-Gonzalez received the M.S. degree in telecommunication engineering from Universidad Politécnica de Madrid (UPM), Madrid, Spain, and the M.S. degree in digital signal processing from the Royal Institute of Technology, Stockholm, Sweden, in 2007. He is currently pursuing the Ph.D. degree with Biomedical Image Technologies Group, UPM.

His current research interests include biomedical image processing, complex systems, and data analysis.

Emmanuel Faure received the Ph.D. degree in complex systems from l'École Politechnique, Paris, France.

He is an Associate Researcher with the California Institute of Technology, Pasadena. He is a Research Engineer with l'École Politechnique, and Technical Co-Director of the Bioemergences platform. His current research interests include machine learning and embryogenesis.

Thierry Savy is a Research Engineer with Complex Systems Institute, Paris, France, and l'École Polytechnique, Paris. He is the Technical Co-Director of the Bioemergences platform. His current research interests include electronics, microscopy, and visualization techniques.

Benoit Lombardot received the Ph.D. degree in physics and integrative biology from l'École Polytechnique, Paris, France.

He is a Researcher with Institut Pasteur Korea, Bundang-gu, Korea. His current research interests include biomechanics and quantitative image analysis.

Jose L. Rubio-Guivernau received the M.S. degree in electrical engineering and computer science from Universidad Politécnica de Madrid (UPM), Madrid, Spain, in 2004. He is currently pursuing the Ph.D. degree with Biomedical Image Technologies Group, UPM.

He is Co-Founder and CTO of Medlumics, a medical device start-up. His current research interests include multiview image reconstruction of biomedical images.

Louise Duloquin received the Ph.D. degree in biology from University Paris 6, Paris, France.

She was trained as an Experimental Embryologist with the Marine Biology Station, Villefranche Sur Mer, France. She is a Research Engineer with the CNRS and Director of the Bioemergences platform for the biological experimentation. Her current research interests include the reconstruction of the sea urchin cell lineage trees.

Maria J. Ledesma-Carbayo received the Ph.D. and M.S. degrees in telecommunications engineering from Universidad Politécnica de Madrid (UPM), Madrid, Spain.

She has been a Visiting Researcher with Oxford University, U.K., Ecole Polytechnique Federal de Lausanne, Switzerland, and the National Institutes of Health, USA. She is an Associate Professor with the Biomedical Image Technologies Group, UPM. Her current research interests include biomedical image analysis, especially cardiac imaging and image guided therapy, and image registration methods.

Paul Bourgine received the Ph.D. degree in economics and cognitive science.

He has been the Director of CREA-Ecole Polytechnique and the National Network on Complex Systems, Paris, France. His current research interests include complex adaptive systems and large interaction networks.

Dr. Bourgine was the Co-Chair of the first Conferences in Economics and Artificial Intelligence in 1986, the first European Conference of Artificial Life in 1990, the first European Conference in Cognitive Economics in 2004, and the European Conference on Complex Systems in 2005.

Nadine Peyrieras received the Ph.D. degree from Pasteur Institute, Paris, France.

She is a CNRS Research Director and Team Leader of the Multiscale Dynamics in Animal Morphogenesis Group. She is the Director of the BioEmergences-IBiSA-France BioImaging Platform. She established and coordinated the EU Project Embryomics providing the first automated and controlled strategies, to achieve the reconstruction of the cell lineage tree in Deuterostomians in 2006. Her current research interests include the reconstruction of living model organisms' multiscale dynamics.

Andres Santos received the M.S. and Ph.D. degrees in telecommunications engineering from Universidad Politécnica de Madrid (UPM), Madrid, Spain.

He is a Full Professor and Director of the Biomedical Image Technologies Group (BIT-UPM). He has been Co-Director of a Master Program on Biomedical Technology and Instrumentation. He has been Coordinator of more than 50 national and international research projects and technology transfer contracts. His current research interests include medical image analysis and acquisition.